Plastic Surface Strain Mapping of Bent Sheets by Image Correlation

by Wei Tong

ABSTRACT—A technique using a single CCD camera, a precision rotation/translation stage, a telecentric zoom lens, and digital image correlation software is described for measuring surface profiles and surface plastic strain distributions of a bent thin sheet. The measurement principles, based on both parallel and pinhole perspective projections, are outlined and the relevant mathematical equations for computing the profiles and displacement fields on a curved surface are presented. The typical optical setup as well as the experimental measurement and digital image correlation analysis procedure are described. The maximum errors in the in-plane and out-of-plane coordinates or displacements are about ±5 and ±25 μm, respectively, and the maximum errors in surface strain mapping are about 0.1% or less based on a series of evaluation tests on flat and curved sample surfaces over a physical field of view of 15.2 × 11.4 mm^2. As an application example, the shape and surface plastic strain distributions around a bent apex of a flat 2 mm thick automotive aluminum AA5182-O sheet, which underwent a 90° bend with three bend ratios of 2*t*, 1*t*, and 0.6*t*, are determined using the proposed technique.

KEY WORDS—3D surface profiling measurement, 3D surface deformation field measurement, sheet metal forming, optical strain mapping method

Introduction

In many sheet metal forming processes, an initially flat sheet metal blank is often stamped into the complex shape of a desired product. The success of such a manufacturing process depends on avoiding severe strain concentrations that may lead to necking and ductile damage of the sheet metals while achieving excellent dimension accuracy of the formed part.[1] Some sheet metal forming operations are primarily in-plane stretching and drawing, but there are many other processes such as bending, flanging, and hemming that result in large out-of-plane displacements over a relatively small lateral dimension, and thus large curvatures and strain concentrations. For example, sharp bending of copper alloy sheets and hemming of steel sheets are widely used in making various electrical connectors and automotive components, respectively.[2,3] Hemming of 5XXX and 6XXX series automotive aluminum alloys is often more problematic (because of surface cracking and shear banding) as these aluminum alloy sheets have lower ductility than low-carbon automotive steel sheets. There is a need to measure the maximum plastic surface strain and strain gradients at the sharp bend apex of formed parts for selecting more suitable aluminum alloys and optimizing the hemming process parameters.[4]

Digital image correlation (DIC) has been increasingly used in recent years for whole-field surface strain mapping applications in many materials and mechanics research laboratories, in part due to the availability of many in-house and commercial software tools.[5–16] Because of the optimization of many factors including the quality of images acquired and the algorithms and parameters adapted in image correlation processing, good reliability and accuracy of the strain mapping results can now be achieved routinely.[16] For strain mapping of the planar deformation and motion of a flat object, the errors in global average strain and local pointwise strain variations can usually be limited to 10 and 100 μstrain or less, respectively.[13,16] Using proper image magnifications and decorated surface contrast patterns, large plastic strains and high strain gradients over small gage dimensions (only a fraction of the original sheet thickness) of the necking region in thin sheets can be easily mapped out in detail.[17] However, when it is necessary to measure the three-dimensional (3D) surface profile and its strain distributions by DIC, an elaborate procedure for camera calibration and lens corrections is usually required.[18–22] In general, a dual-camera imaging system is used and the calibration of each camera is carried out by a nonlinear optimization of about 10 or more intrinsic and extrinsic parameters using precision square grids or cross-line gratings and multiple out-of-plane translations.[19,20] When a single camera system is adopted, the additional calibration of the projector[18] or multiple in-plane translations[21] may be used. Again, multiple image correlation processing steps and a nonlinear optimization procedure are required to estimate the 10 or more camera parameters. When the 3D surface profile is known to be cylindrical and the deformation is symmetric about the cylindrical axis, a single camera imaging system with minimum calibration requirements has also been used for surface strain mapping.[22]

Here we present a simpler technique for measuring both the surface profile and its surface plastic strain distributions of a 3D object using a single camera imaging system with a telecentric zoom lens and a rotation/translation stage. In the following, the measurement principles, based on both parallel and pinhole perspective projections, are first described. The feasibility of the proposed technique is then assessed through a set of evaluation tests. The experimental procedure and results are given in detail for both surface profiling and surface strain mapping measurements. The measurement errors are

W. Tong (SEM member; wei.tong@yale.edu) is an Associate Professor, Department of Mechanical Engineering, Becton Engineering Center, Yale University, New Haven, CT 06520-8282 USA.

Original manuscript submitted: November 19, 2003.
Final manuscript received: May 11, 2004.
DOI: 10.1177/0014485104047384

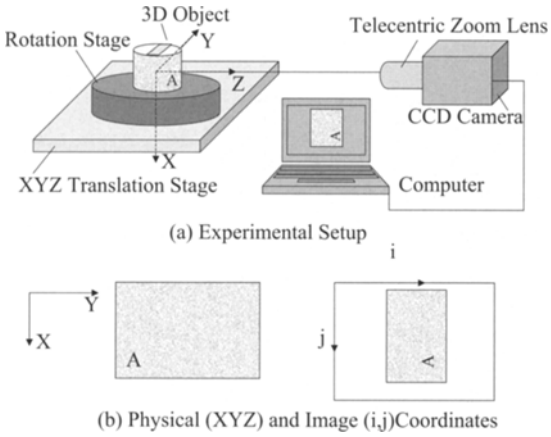

Fig. 1—Typical optical setup (a) and definitions of the physical and image coordinate systems (b) used for 3D surface profiling and strain mapping measurements. The letter "A" on the 3D object (a cylindrical rod) is used to illustrate the object orientation in the digital images

assessed and the robustness of the technique is discussed in terms of its tolerance for misalignments of the optical setup and the uncertainty of the rotation angle readouts. Finally, the advantages of using a single camera system for 3D surface profiling and strain mapping are elucidated and potential applications of the proposed technique in sheet metal forming research are emphasized through an example of a bent automotive aluminum sheet.

Measurement Principles

The measurement principles based on both parallel and pinhole projections are described in this section, and the relevant mathematical equations for computing the 3D surface profiles and displacement fields are derived.

Optical Setup and the Two Coordinate Systems

Figure 1 shows a typical measurement setup consisting of a combined rotation and translation specimen stage, a telecentric zoom lens, a CCD camera, and a computer (for acquiring digital images from the camera and for image processing and data analysis). It is assumed that the optical axis of the imaging system is parallel with the Z-axis of the specimen stage and a flat object with its surface aligned with the XY-plane on the specimen stage is imaged digitally with pixel coordinates (i, j); see Fig. 1(b). The intercepting point between the XY-plane and the optical axis defines the origin of the physical coordinate system ($X = Y = Z = 0$). It is not necessary that the optical axis should intercept the axis of the rotation stage (but the rotation axis should be parallel with the X-axis of the physical coordinate system and lies within the XY-plane).

Surface Profiling by the Parallel Projection Method

A parallel projection is usually assumed when an image is formed by scanning optical means (such as the secondary electron images obtained in a scanning electron microscope; see Brandon and Kaplan[23]). If one uses a telecentric lens and maintains a long effective object-to-lens distance in the conventional optical image formation (see Fig. 1), a parallel projection may also be an excellent approximation. The measurement consists of taking digital images of a sample placed on the rotation stage platform at three different orientations, as shown in Fig. 2(a). With the distance between a point A on the 3D sample surface and the rotation axis O (assumed parallel with the X-axis) being R, the angle between the line OA and the Z-axis being α, and the magnitude of both positive (from OA to OA^+) and negative (from OA to OA^-) rotations being θ, we can write the physical coordinates of the same surface point at the three different orientations based on three recorded digital images as (see Fig. 2(b))

$$\begin{cases} X = \eta\beta\,(i - i_0)\,, \\ Y = -\beta\,(j - j_0) = R\sin\alpha, \\ Z = R\cos\alpha, \end{cases} \tag{1a}$$

$$\begin{cases} X^+ = \eta\beta\,(i^+ - i_0)\,, \\ Y^+ = -\beta\,(j^+ - j_0) = R\sin(\alpha + \theta)\,, \\ Z^+ = R\cos(\alpha + \theta)\,, \end{cases} \tag{1b}$$

$$\begin{cases} X^- = \eta\beta\,(i^- - i_0)\,, \\ Y^- = -\beta\,(j^- - j_0) = R\sin(\alpha - \theta) \\ Z^- = R\cos(\alpha - \theta)\,, \end{cases} . \tag{1c}$$

Here, (i, j),(i^+, j^+), and (i^-, j^-) are the pixel coordinates of the digital image projections k, k^+, and k^- of the surface point at three orientations A, A^+, and A^-, (i_0, j_0) are the pixel coordinates of the image center, β is the digital image pixel scale in the vertical direction of digital images (i.e., the physical dimension of an object along the Y-axis per pixel), and η (>0) is the average aspect ratio of the vertical dimension over the horizontal dimension of pixels (accounting for possible non-square pixels of digital images). Through some algebraic manipulations, we can determine the Z-coordinate as

$$Z = \frac{Y^+ - Y^-}{2\sin\theta} = -\frac{\beta\,(j^+ - j^-)}{2\sin\theta} = -\frac{\beta\Delta j}{2\sin\theta}. \tag{2}$$

In summary, by recording three images of the sample at three different orientations of the rotation stage, we can measure the surface profile of the sample by (assuming even that there is an offset (Y_0, Z_0) between the rotation axis and the X-axis)

$$\begin{cases} X = \eta\beta\,(i - i_0)\,,\ Y - Y_0 = -\beta\,(j - j_0)\,, \\ Z - Z_0 = -\frac{\beta(j^+ - j^-)}{2\sin\theta} = -\frac{\beta\Delta j}{2\sin\theta}. \end{cases} \tag{3}$$

Surface Profiling by the Pinhole Projection Method

The optical setup shown in Fig. 1 can be better described by a pinhole perspective projection model [18–21] for a video camera/lens unit; see Fig. 3. The schematics without and with an offset (Y_0, Z_0) between the rotation axis and the X-axis are shown as cases a and b in Fig. 3, respectively. Again, we can write the physical coordinates of the surface point at three different orientations based on the recorded images and pinhole projection image formation as

$$\begin{cases} X = \eta\beta\,(i - i_0)\,(1 - Z/D_0)\,, \\ Y - Y_0 = -\beta\,(j - j_0)\,(1 - Z/D_0) = R\sin\alpha, \\ Z - Z_0 = R\cos\alpha, \end{cases} \tag{4a}$$

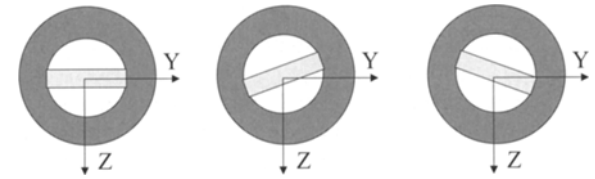

(a) Three Rotation Stage Positions for 3D Measurements

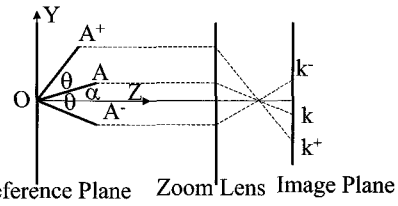

(b) The Corresponding Image Formation by Parallel Projection

Fig. 2—Schematic diagram of three orientations of the rotation stage used for 3D surface profiling measurements by parallel projection. A small rectangular strip on the top of the cylindrical rod, as shown in Fig. 1(a), is used to indicate the object orientation relative to the rotation stage

$$\begin{cases} X^+ = \eta\beta\left(i^+ - i_0\right)\left(1 - Z^+/D_0\right), \\ Y^+ - Y_0 = -\beta\left(j^+ - j_0\right)\left(1 - Z^+/D_0\right) = R\sin\left(\alpha + \theta\right), \\ Z^+ - Z_0 = R\cos\left(\alpha + \theta\right), \end{cases} \tag{4b}$$

$$\begin{cases} X^- = \eta\beta\left(i^- - i_0\right)\left(1 - Z^-/D_0\right), \\ Y^- - Y_0 = -\beta\left(j^- - j_0\right)\left(1 - Z^-/D_0\right) = R\sin\left(\alpha - \theta\right) \\ Z^- - Z_0 = R\cos\left(\alpha - \theta\right), \end{cases} \tag{4c}$$

Here, (Y_0, Z_0) is the location of the rotation axis (O' in Fig. 3(b)), D_0 is the effective distance between the reference plane (the XY-plane of the physical coordinate system) and the lens, and β is the digital image pixel scale that is defined here as the physical dimension along the Y-axis of an object at the observation depth $Z = 0$ per pixel. If we know the offset (Y_0, Z_0) between the rotation axis O' and the origin of the physical coordinate system O, we can solve for (X, Y, Z) from the following equations

$$\begin{cases} X = \eta\beta\left(i - i_0\right)\left(1 - Z/D_0\right), \\ -\beta\left(j^+ - j_0\right)\left\{D_0 - \left(Z - Z_0\right)\cos\theta + \left(Y - Y_0\right)\sin\theta\right\} \\ = D_0\left(Y - Y_0\right)\cos\theta + D_0\left(Z - Z_0\right)\sin\theta, \\ -\beta\left(j^- - j_0\right)\left\{D_0 - \left(Z - Z_0\right)\cos\theta - \left(Y - Y_0\right)\sin\theta\right\} \\ = D_0\left(Y - Y_0\right)\cos\theta - D_0\left(Z - Z_0\right)\sin\theta, \end{cases} \tag{5}$$

or

$$\begin{cases} X = \eta\beta\left(i - i_0\right)\left(1 - \frac{Z}{D_0}\right), \\ Y = Y_0 + \dfrac{-\beta\left(j^+ + j^- - 2j_0\right)\sin\theta}{\left[1 + \left(\beta/D_0\right)^2\delta j\right]\sin 2\theta - \beta/D_0\,\Delta j\cos 2\theta}, \\ Z = Z_0 + \dfrac{-\beta\,\Delta j\cos\theta + 2\beta^2/D_0\,\delta j\sin\theta}{\left[1 + \left(\beta/D_0\right)^2\delta j\right]\sin 2\theta - \beta/D_0\,\Delta j\cos 2\theta}, \end{cases} \tag{6}$$

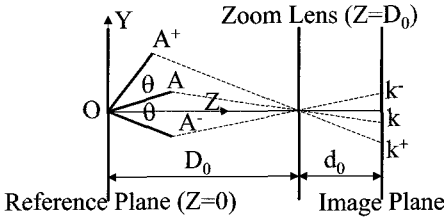

(a) Image Formation by Pinhole Projection (Zero Offset)

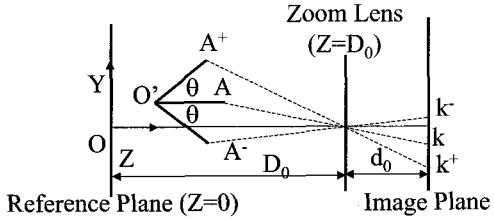

(b) Image Formation by Pinhole Projection with Offset

Fig. 3—Schematic diagram of 3D surface profiling measurements by pinhole projection: (a) the rotation axis of the stage coincides with the point "O" (the intersection of the camera optical axis with the X–Y plane); (b) the rotation axis of the stage is located at the point O' with a coordinate of (Y_0, Z_0). Note that the rotation axis of the stage is assumed to be parallel with the X-axis (see Fig. 1(a)). The parameter d_0 is the effective focal length of the camera unit in a pinhole camera model

where $\Delta j = j^+ - j^-$ and $\delta j = \left(j^+ - j_0\right)\left(j^- - j_0\right)$. If there is a significant offset component Z_0, it may be determined by combining eqs (4) and (6)

$$Y - Y_0 = Y' = -\beta\left(j - j_0\right)\left(1 - \frac{Z_0 + Z'}{D_0}\right), \tag{7}$$

or

$$Z_0 = D_0 - Z' + \frac{D_0 Y'}{\beta\left(j - j_0\right)}, \tag{8}$$

where $Y' = Y - Y_0$ and $Z' = Z - Z_0$ are given in eq (6). If $Z_0 = 0$ or $Z_0/D_0 \ll 1$, we can compute $(Y - Y_0)$ from the second equation in both eqs (4) and (6) and the difference may be used to assess the validity of the pinhole perspective projection model or the amount of the telecentric zoom lens distortion. When $\beta/D_0 \ll 1$, eqs (6) are reduced to eqs (3).

Measurements of Surface Displacement Fields

We can determine the surface displacement distributions of a 3D object by measuring the surface profiles before and after the object undergoes deformation and rigid-body motion using the same optical setup (for simplicity, assume the same rotation angles are used in both measurements). Using the three images acquired at three different orientations of the object after deformation and motion, we can compute the new physical coordinates $(\tilde{X}, \tilde{Y}, \tilde{Z})$ of a surface point by

using eq (6) as

$$\begin{cases} \tilde{X} = X + U = \eta\beta\left(\tilde{i} - i_0\right)\left(1 - \frac{\tilde{Z}}{D_0}\right), \\ \tilde{Y} = Y + V = Y_0 + \frac{-\beta(\tilde{j}^+ + \tilde{j}^- - 2j_0)\sin\theta}{\left[1+(\beta/D_0)^2\delta\tilde{j}\right]\sin 2\theta - \beta/D_0\Delta\tilde{j}\cos 2\theta}, \\ \tilde{Z} = Z + W = Z_0 + \frac{-\beta\Delta\tilde{j}\cos\theta + 2\beta^2/D_0\delta\tilde{j}\sin\theta}{\left[1+(\beta/D_0)^2\delta\tilde{j}\right]\sin 2\theta - \beta/D_0\Delta\tilde{j}\cos 2\theta}. \end{cases} \tag{9}$$

Here, $(\tilde{i}, \tilde{j})$, $(\tilde{i}^+, \tilde{j}^+)$, and $(\tilde{i}^-, \tilde{j}^-)$ are the image pixel coordinates of the deformed surface point at three different orientations of the rotation stage, and $\Delta\tilde{j} = \tilde{j}^+ - \tilde{j}^-$, $\delta\tilde{j} = (\tilde{j}^+ - j_0)(\tilde{j}^- - j_0)$. Surface strains can then be computed based on the six in-plane gradients of these three Lagrangian displacements U, V, and W (see the appendix in Tong[11]).

Tracking Image Pixel Coordinates by Digital Image Correlation

As shown in the previous sections, the key to realizing accurate measurements of surface profiles and surface displacement fields is to know precisely the pixel coordinates of the image projection k, k^+, and k^- of a surface point at different rotation orientations A, A^+, and A^-. Fortunately, the image pixel coordinates after an object undergoes motion and deformation can be easily determined with subpixel accuracy by DIC.[5–16] A sum-squared-difference correlation coefficient accounting for variations in the local average brightness and contrast, a typical subset of 40 × 40 pixels, and a grid spacing of 10 pixels in both directions were used in the following image correlation analysis. Details of DIC and its specific implementation in a surface deformation-mapping program SDMAP used in this investigation are given elsewhere.[14,15]

Experimental Procedures and Results

Several evaluation tests have been carried out to assess the feasibility of the proposed technique for accurately measuring surface profiles and surface displacement fields of a 3D object. The experimental procedure and results of these tests are described in the following.

Experimental Setup

A simple optical configuration was set up on an optical table following very closely the schematic diagram shown in Fig. 1. The specimen stage consisted of a rotation stage (Newport Model 481-A) mounted on top of a matching *XYZ* translation stage (Newport Model 460A). The rotation stage had a resolution better than 0.01° and a fine adjustment range of 5°. The translation stage had a maximum travel of 13 mm along each axis, a minimal incremental motion of about 1 μm, and the maximum angular deviation between axes of the translation stage was less than 0.01°. The zero degree position of the rotation stage was aligned with the *XY*-plane of the XYZ translation stage. A 0.5 inch high-resolution black-and-white CCD video camera (Model OS-40D, Mintron Enterprise USA) was mounted facing the combined rotation/translation stage at the other end of the optical table. A Computar 55mm F/2.8 telecentric zoom lens (Edmund Scientific Co.) was attached to the CCD camera. A desktop computer with a variable scan monochrome PCI frame grabber (Model DT3152, Data Translation, Inc.) was used to acquire 640 × 480 8-bit grayscale digital images from the CCD camera NSTC video output. Each image was acquired by averaging over a total of 60 video frames so the intrinsic noises in the digital images could be reduced significantly.[13] A DIC software package SDMAP, developed at Yale University, was also installed on the computer for image correlation processing and data analysis.[14,15]

A proper camera alignment was crucial for accurate and reliable 3D measurements using the proposed technique here: (a) the optical axis of the camera-lens unit should be perpendicular to the *XY*-plane defined by the XYZ translation stage; (b) the rotation axis should be parallel with the *X*-axis of the coordinate system; (c) the rotation axis should lie on the *XY*-plane (see Fig. 1 for the definitions of both the physical and image coordinate systems). The alignment step (a) was carried out first by visual inspection of the image of a precision square grid pattern. The grid pattern was attached to a flat block that was mounted on the rotation stage platform and the surface of the flat block was set to be parallel with the *XY*-plane of the stage. We first adjusted roughly both the camera and stage until there was no apparent distortion of the grids in the images. The fine adjustment was then performed with the help of the *Z*-axis translation of the sample stage. We acquired the digital images of the grid pattern before and after a translation in the *Z*-direction and then obtained the image displacement map between them using DIC. An excellent alignment was achieved when the image center had no or very little displacement upon a finite *Z*-axis translation. The alignment steps (b) and (c) were realized by using a rotation stage that was specifically designed to mount concentrically onto the XYZ-translation stage (such as the Newport stages used here).

The digital image scale β was determined by placing an object with a known dimension along the *Y*-axis at the reference plane position ($Z = 0$) and recording a digital image of the object. The camera/lens unit used in the tests has an image pixel scale β of 0.024 mm pixel^{-1}. The pixel aspect ratio of digital images used in this study was determined to be $\eta = 1.01634 \pm 0.00095$ based on four in-plane rotation tests.[21] The effective object-to-lens distance D_0 used for the pinhole projection method was obtained by recording two images of a flat object before and after a *Z*-axis translation W_0. The flat object had a fine random contrast pattern and was placed at the reference plane ($Z = 0$) before the translation. The average displacement gradients $\bar{u}_x$ and $\bar{v}_y$ between the two images were computed by the DIC program SDMAP and the effective object-to-lens distance of the pinhole camera model was given by

$$D_0 = W_0\left(1 + \frac{2}{\bar{u}_x + \bar{v}_y}\right). \tag{1}$$

A flat object with a random contrast pattern was translated 0.05 inch (1.27 mm) both towards and away from the camera and three digital images were recorded. The average displacement gradient of the two image pairs was 0.001648. Consequently, the estimated effective object-to-lens distance D_0 was 771.9 mm. The apparent working distance of the lens was measured to be about 155 mm from the *XY*-plane and the much larger value of D_0 (almost five times the lens working distance) reflects the telecentric characteristics of the zoom

lens used. Finally, the pixel coordinates of the ideal digital image center were chosen to be simply $(i_0, j_0) = (320,240)$ for the 640 × 480 grayscale digital images used in these evaluation tests. We can also measure directly the image center coordinates of the camera/lens unit by recording two images of a flat object placed on the specimen stage before and after zooming (instead of a translation in the Z-axis of the XYZ translation stage). The image center is the image point where there is zero displacement. A zooming test was conducted and the image center was found to be (318.6, 235.5), which is rather close to the ideal case of (320, 240).

Profiling of a Flat Surface

The first evaluation test was carried out to measure the surface profile of a flat copper block (25 × 25 × 5 mm^3) placed on the platform of the rotation stage. This test was used to assess the errors in out-of-plane topography measurements and to compare the difference in results between the parallel and pinhole projections. As shown in Fig. 4(a), three images of the copper block were acquired with the rotation stage at 0°, +10°, and −10° positions, respectively. The copper block surface was sprayed with fine and random black-and-white paint speckles. The three images were first processed consecutively by the DIC program SDMAP and the image coordinates (i, j),(i^+, j^+), and (i^-, j^-) of the flat surface were saved to a file. The SDMAP program was then used to further process the data using eq (3) or eq (6) to generate the surface profile data set after supplying the required input parameters (the image scale β, the image center (i_0, j_0), the effective object-to-lens distance D_0, and the rotation angle θ).

The surface profiling results are shown in Figs. 4(b) and (c). The measurement shows that the surface is indeed rather flat (the standard deviation from a flat surface is about 2–3 μm and is of the same order of the surface roughness of the copper block) but is tilted slightly from the reference plane ($Z = 0$); the tilt angles between the flat surface and the X-axis and Y-axis are about 1.4° and 1.9°, respectively. The maximum differences between the results by parallel projection and the results by pinhole projection are respectively 3, 2, and 23 μm for the three physical coordinates. These differences are only slightly above the uncertainty of the measurement system (the combined errors in rotation angles and image correlation are estimated to be approximately 1–2 μm for the X and Y coordinates and less than 10 μm for the Z coordinates). The relatively small differences in results between these two projection methods reflect the effectiveness of the telecentric zoom lens used in the camera setup (here $|Z| / D_0 \leqslant 1/1800$).

Profiling of a Cylindrical Surface

The second evaluation test was carried out to measure the profile of a cylindrical surface of an aluminum block (25 × 20 × 10 mm^3). The aluminum block surface was also sprayed with fine and random black-and-white paint speckles. The three digital images acquired with the rotation stage at 0°, +10°, and −10° orientations are shown in Fig. 5(a). Following the procedure described in the previous section, the surface profiling results can be obtained by the SDMAP program and are summarized in Figs. 5(b) and (c). Again, little point-by-point difference (at most 13–23 μm) is found between the profiling results by the parallel projection (eq (3)) and the profiling results by pinhole projection (eq (6)). The measured surface profile matches the cross-sectional shape (YZ-plane) of the aluminum block rather well (see Fig. 6).

3D Surface Strain Mapping Calibrations

The third evaluation test was performed to assess the error levels in surface strain mapping upon the rigid-body motion of the flat copper block used earlier. In addition to the three images described earlier in the section *Profiling of a Flat Surface*, the copper block was rotated to $\theta = -5°$ position as the "deformed" shape. Three images were then taken with the copper block at positions of $\theta = -5°$, +5°, and −15°, respectively. The six images of the original and rotated copper block constituted the required image set for 3D surface strain mapping measurements. The six images were processed again consecutively by the DIC program SDMAP and the image coordinates (i, j),(i^+, j^+),(i^-, j^-),$(\tilde{i}, \tilde{j})$, $(\tilde{i}^+, \tilde{j}^+)$, and $(\tilde{i}^-, \tilde{j}^-)$ of the copper block were saved to a file. The SDMAP program was then used to further process the data file to generate the surface profiling and strain mapping data set using eqs (6) and (9) after supplying the required input parameters: the image scale β, the image center (i_0, j_0), the effective object-to-lens distance D_0, and the rotation angle θ.

The 3D surface displacement fields upon rotating the copper block ($\theta = -5°$) are shown in Fig. 7(a) and the corresponding surface strain mapping results are presented in Fig. 7(b). The local strain levels over the entire three maps range from 0.03% (E_x component) to 0.1% (E_y component). The average strains over the entire maps are $E_{xave} = 8 \times 10^{-6}$, $E_{xyave} = 248 \times 10^{-6}$, and $E_{yave} = -361 \times 10^{-6}$, respectively. As the copper block only rotates about the X-axis without deformation, these strains can be treated as the error levels of the measurements using the current camera/lens unit and rotation/translation stage alignments.

Surface Strain Mapping of a Bent Aluminum Sheet

Finally, the proposed technique was applied to measure the plastic surface strain distributions of a flat sheet metal piece after 90° sharp bending. A flat aluminum AA5182-O sheet (50 mm long, 25 mm wide, and 2 mm thick) printed with random permanent ink patterns on its surface was first digitally imaged at three rotation stage orientations (see Fig. 8(a)). Using a special wrap-type sheet metal bending apparatus (Olin Metal Research Labs, New Haven, CT; see also Mandigo[2] for details), the aluminum sheet was then subjected to a 90° bend with a radius $r = 2$ mm along the Y-axis (the so-called bend ratio r/t was 1 or $r = 1t$, where t is the sheet thickness). The bent aluminum sheet, with its bend apex facing the camera, was then imaged again at three rotation stage orientations (see Fig. 8(b)). The use of the permanent ink pattern was preferred over the conventional sprayed paint speckles because the permanent ink patterns were found to be more resistant to cracking and decohesion after large straining at the bend apex. Digital images of the ink patterns on the bent aluminum sheet, as shown in Fig. 8(b), remained of high quality with no apparent degradation.

Following the procedure described in the previous section, the six images of the aluminum sheet were processed consecutively by the DIC program SDMAP and the image coordinates of the aluminum sheet after rotation and bending were saved to a data file. The SDMAP program was then

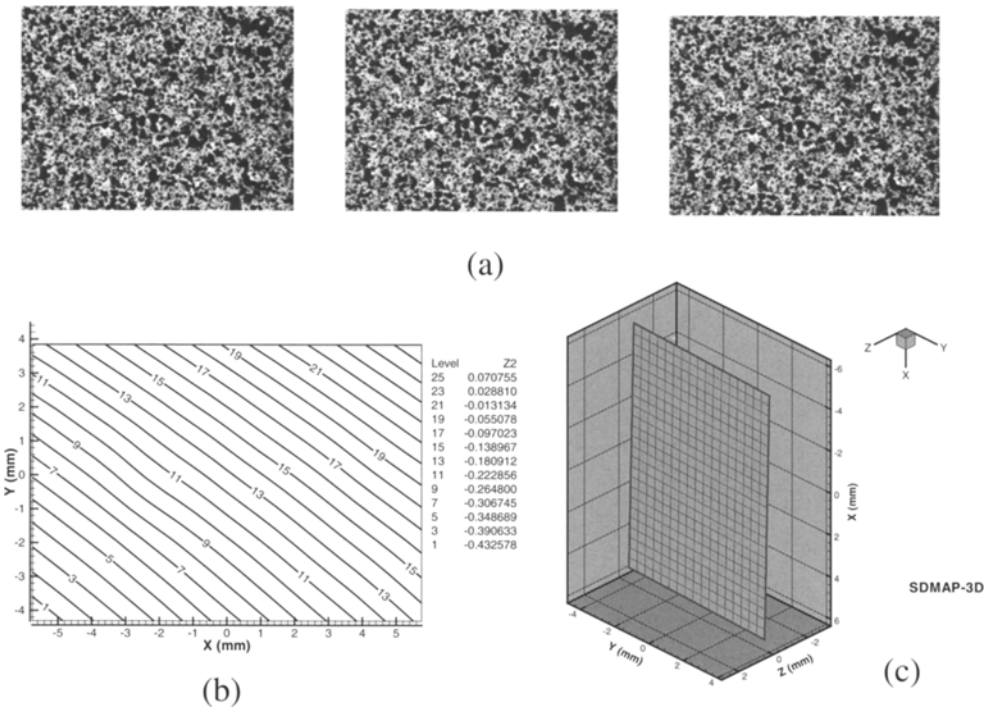

Fig. 4—Three digital images used to measure the profile of a flat copper block surface with $\theta = 0°$, $+10°$, and $-10°$ (a). The field of view of these images is 15.4 × 11.5 mm^2. The measured surface profile $Z(X,Y)$ of the flat copper block is shown as a contour plot (b) and a surface topography plot (c)

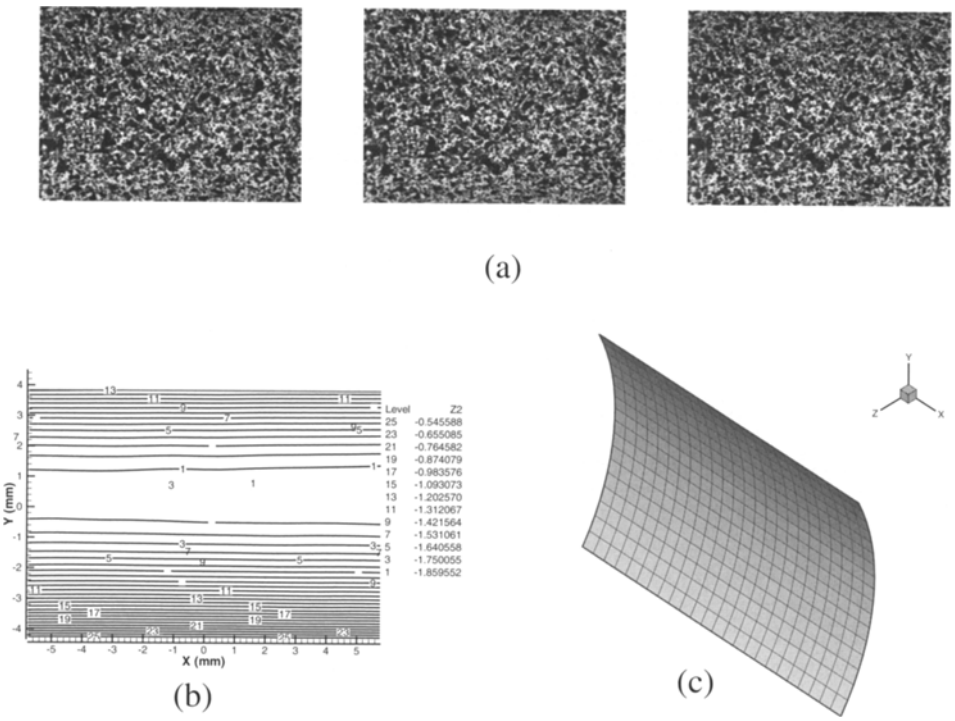

Fig. 5—Three digital images used to measure the profile of a cylindrical surface of an aluminum block with $\theta = 0°$, $+10°$, and $-10°$ (a). Measured surface profiling results of the cylindrical surface of an aluminum block are given as a contour plot (b) and a topography plot (c)

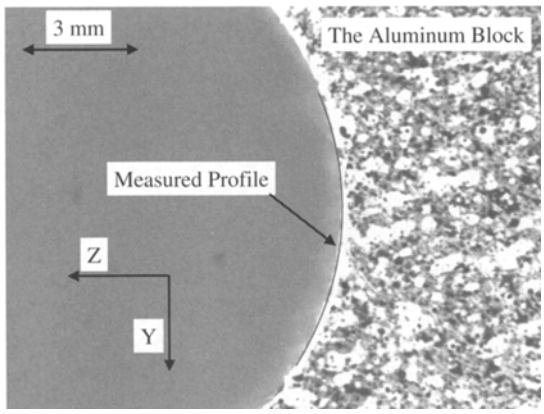

Fig. 6—Comparison of the measured surface profile $Z(X,Y)$ at a fixed X and the cross-sectional side view of the aluminum block

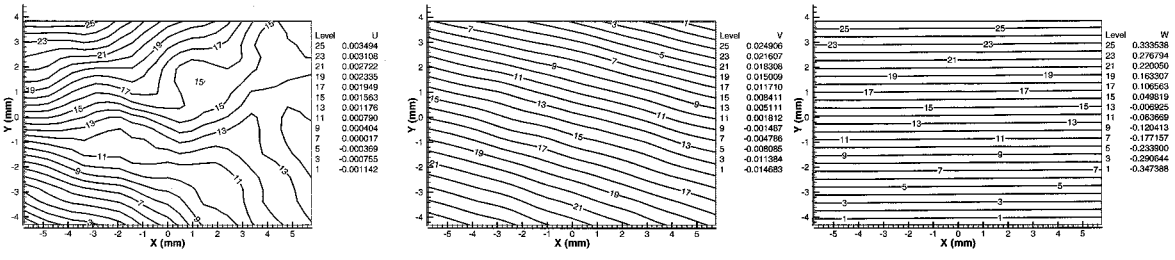

(a) The 3D Displacement Contour Plots

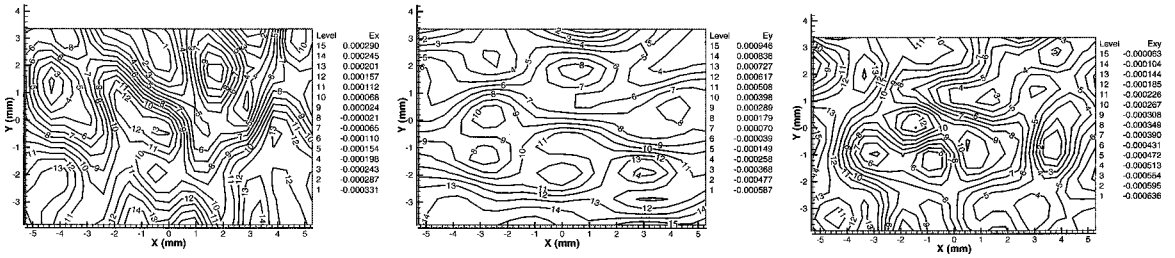

(b) The In-Plane Surface Strain Contour Plots

Fig. 7—(a) Measured 3D surface displacement fields of a flat copper block after a 5° rotation about the X-axis (units in mm). (b) In-plane surface strain mapping results upon the 5° rotation of the flat copper block

used to further process the data file based on the pinhole projection method to generate the surface profiling and strain mapping data set after supplying the required input parameters. The shape of the bent aluminum sheet is found to be similar to that of a cylindrical surface (see Fig. 9(a)). The measured profile along the Y-axis is found to match very closely the side-view shape of the bent aluminum sheet (Fig. 9(b)). The surface strain mapping results (the true strain component E_y) are presented in Fig. 10 as (a) a two-dimensional (2D) strain map and (b) a one-dimensional (1D) distribution profile across the bend apex. The plastic strain component E_y across the bend apex is found to be non-uniform and the maximum true strain at the bend apex is about 33.9% for the bend ratio of $1t$. The normal strain along the X-axis (perpendicular to the bend) and the shear strain in the XY-plane are 0.4% or less at the bend apex, indicating that the bend apex surface is in a predominantly plane strain state. The aluminum sheet was bent with two other radii of 4 and 1.2 mm, respectively, and the resulting distributions of the true strain component E_y are shown in Figs. 10(c) and (d). The maximum true strains at the bend apex are about 21.3% and 39.2%, respectively, for the bend ratios of $2t$ and $0.6t$.

Discussion

By placing a rotation stage concentrically on a XYZ translation and using a telecentric zoom lens that is commonly

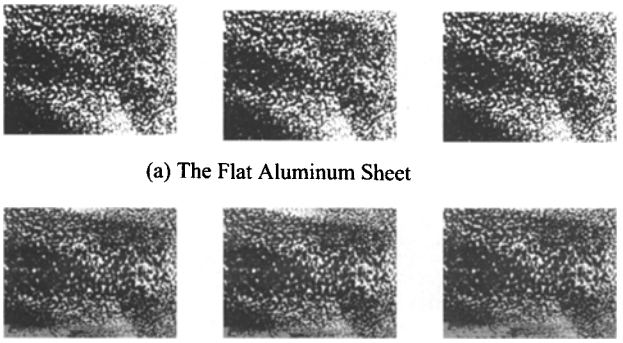

(a) The Flat Aluminum Sheet

(b) The Bent Aluminum Sheet

Fig. 8—Three digital images of a flat aluminum sheet (a) and the three digital images after the aluminum sheet was bent with a bend ratio of 1*t* (b) acquired at three rotation stage orientations (θ = 0°, +5°, and −5°). This set of six images was used to measure both the profile and plastic surface strain distributions around the bend apex region

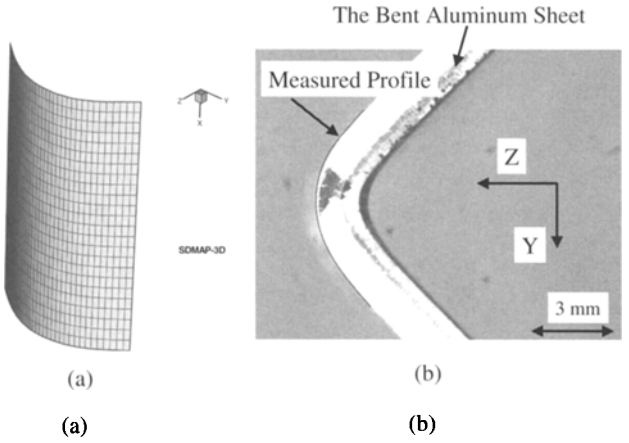

(a) (b)

Fig. 9—Measured surface profiling results of the bent aluminum sheet with a bend ratio of 1*t*: (a) topography plot; (b) comparison of the measured surface profile $Z(X,Y)$ at a fixed X and the cross-sectional side view of the bent aluminum sheet

adapted in machine vision applications, the proposed 3D surface profiling and strain mapping technique achieves nearly the parallel projection condition found commonly in scanning microscopy.[23,24] It completely avoids the nonlinear optimization process of determining the camera parameters and the associated multiple translations and image processing steps. Both the alignment and calibration of the optical setup are more easily accomplished using off-the-shelf optical components and a DIC program. The concentric positioning of the rotation stage (i.e., its rotation axis is aligned with the X-axis of the physical coordinate system defined by the camera/lens and it lies within the XY-plane so $Z_0 = 0$ or more practically $Z_0/D_0 \ll 1$) is the most critical part of the optical setup of this technique. The residual errors of the measurements should be primarily due to the second-order distortion of the telecentric zoom lens. The overall errors in both profiling and strain mapping of curved surfaces of a given optical setup can be quickly assessed following the examples described in the previous sections. The effects of the lens distortion, the image center offset, rotation angle errors, and small optical misalignments on the accuracy of 3D surface profiling and strain mapping measurements are further discussed here.

By profiling and strain mapping a flat surface described in the previous section, the lens distortion can be examined by comparing the difference in $(Y - Y_0)$ computed using the second equation in both eq (4) and eq (6). It is found that the difference in $(Y - Y_0)$ is rather small (the average value is only 0.5 μm) and increases with the distance away from the optical axis (the image center). Small image center offsets of 5–10 pixels (due to the error mounting the zoom lens onto the CCD camera, etc.) do not affect greatly the accuracy of the profiling measurements. By varying the image center coordinates within ±10 pixels during the post data processing, only small but mostly constant shifts in the X, Y, and Z coordinates of up to 200, 200, and 5 μm are detected, respectively (similar to an in-plane rigid body translation). The displacement gradients induced are negligible (e.g., dW/dY is about 0.006% or 60 μm mm^{-1} per off-center pixel). When a 0.5° error is assumed in the rotation angle readout, small variations in the X, Y, and Z coordinates of about 1, 5, and 2 μm are detected, respectively. The in-plane displacement gradients induced are negligibly small but the out-of-plane displacement gradient component dW/dY (the profile slope change) is about 0.2–0.3% (i.e., 5–6 μm mm^{-1} per degree). Recalling that the Newport Model 481-A rotation stage has a resolution better than 0.01°, the uncertainty in rotation angles of 0.1° or less can be realized in the experiments. As only the square of dW/dY is used for computing the in-plane surface strains (see the appendix in Tong[11]), so the error in surface strains due to the uncertainties in rotation angles of even 1° is less than 0.004%.

One of the major sources of error in strain mapping may be due to the fact that the flat surface of an undeformed object may have some tilt from the reference XY-plane initially. In other words, the true specimen coordinate system $x'y'z'$ defined in terms of the flat surface may not coincide with the coordinate system defined by the camera/lens unit. A tilt of 2° can indeed induce an error of about 0.2–0.3% in strains. Nevertheless, the tilt angles can be determined from the profiling measurement of the flat surface before the bending operation and the tilt effect of the flat surface can be easily corrected by a simple 3D coordinate transformation between the two coordinate systems XYZ and $x'y'z'$. The strain errors can thus be reduced to the level of ±0.02% or less.

Both the image pixel scale β and the effective object-to-lens distance D_0 can be determined within an accuracy of 0.05% or better with the aid of image correlation and they have minimal effects on the accuracy of both profiling and strain mapping measurements. If the digital image pixels are far from squares and the measurement object undergoes some in-plane rotation or shearing, then the aspect ratio value of pixels is needed in the image processing step to reduce errors in strains. Calibration of the average aspect ratio of the digital image pixels can be performed following the simple procedure suggested elsewhere.[15,21] The pixel aspect ratio of digital images used in this study was determined to be $\eta = 1.01634 \pm 0.00095$ based on four in-plane rotation tests. The effects of non-square pixels were automatically corrected during the image correlation processing step of the data analysis using the in-house built software SDMAP.

Compared with most of the dual camera optical setups for 3D surface profiling and strain mapping applications, the

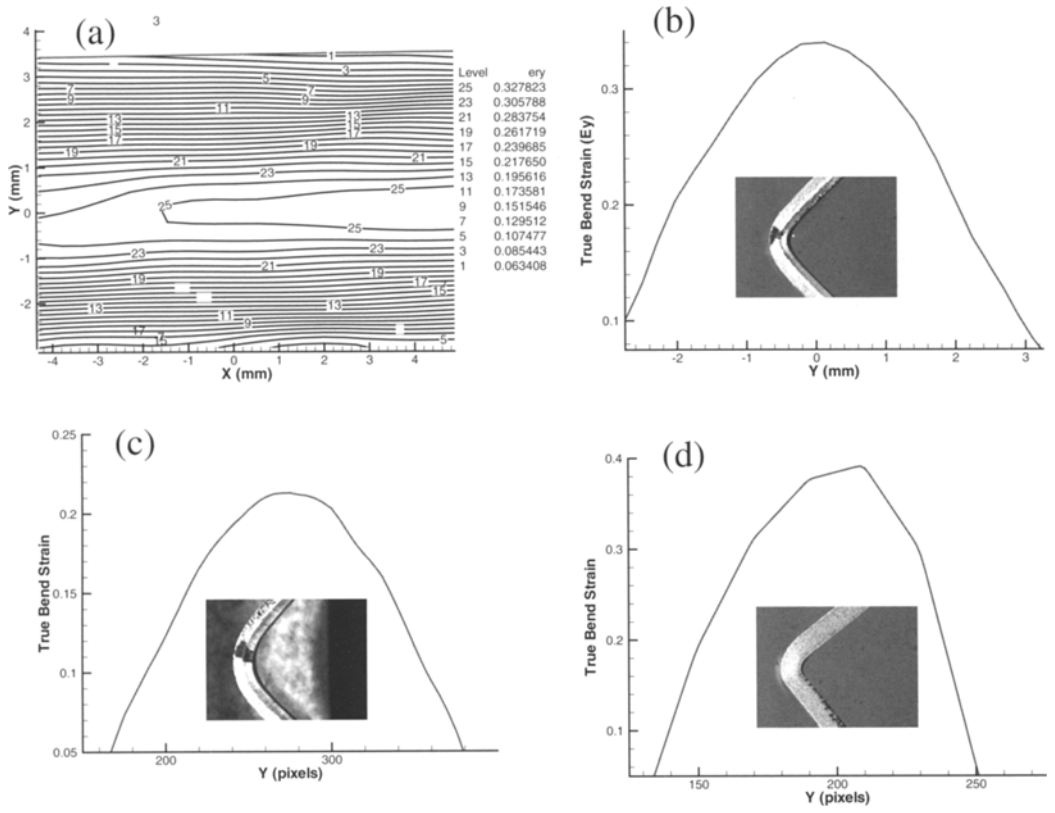

Fig. 10—The measured true bend strain distributions around the apex of the bent aluminum sheet: (a) 2D mapping results (bend ratio = 1t); (b) 1D profile of the bend strain variations across the bend apex (X = 2.3mm, bend ratio = 1t); (c) 1D profile of the bend strain variations across the bend apex (bend ratio = 2t); (d) 1D profile of the bend strain variations across the bend apex (bend ratio = 0.6t). The side views of the three bent aluminum sheet samples are also shown in (b)–(d)

single camera system described here has many advantages, including the capability for close-up applications (a smaller field of view and higher spatial resolution of the strain fields and sharper profiles), fewer requirements on hardware and alignments, and reduced errors due to the camera-to-camera difference. The software implementation of the proposed technique can also be used for microscale profiling and strain mapping applications using scanning optical microscopy and scanning electron microscopy.[23,24]

Conclusions

A simple technique based on a rotation/translation stage and a telecentric zoom lens has been shown to be able to measure accurately the surface profile and plastic strain distribution of a 3D bent sheet by either the parallel or pinhole projection methods. The maximum errors in the in-plane and out-of-plane coordinates or displacements are about ±5 and ±25 μm, respectively. These correspond to about 0.2 and 1 pixel or about 0.026% and 0.13%, respectively, of the diagonal dimension of the imaged region. Upon the correction for the tilt of the initially flat surface, the maximum errors in surface strain mapping are found to be about 0.1% or less. The proposed technique is particularly suitable for measuring plastic strain distributions around sharp bends in many sheet metal forming applications.

Acknowledgments

Mr Eric Rocco of Yale University helped to perform the 3D measurements reported here. Dr Frank N. Mandigo of Olin Metals Research Laboratory (New Haven, CT) provided both valuable advice and direct assistance in carrying out bending tests of aluminum sheets using a wrap-type sheet metal bending apparatus at Olin. The aluminum sheet samples (AA5182-O) used in the surface strain measurements were provided by Dr Wayne Cai of GM R&D Center (Warren, MI).

References

1. *Hosford, W.F. and Caddell, R.M., Metal Forming: Mechanics and Metallurgy, 2nd edition, Prentice-Hall, Englewood Cliffs, NJ (1993).*
2. *Mandigo, F.N., "Bending Ductility Tests," ASM Metals Handbook, Vol. 8, ASM, Metals Park, OH, 125–131 (1985).*
3. *Muderrisoglu, A., Murata, M., Ahmetoglu, M.A., Kinzel, G., and Taylan, T., "Bending, Flanging, and Hemming of Aluminum Sheet – An Experimental Study," Journal of Materials Processing Technology,* **59***(1–2), 10–17 (1996).*
4. *Friedman, P.A. and Luckey, S.G., "Bendability of Al–Mg–Si Sheet Alloys For Automotive Closure Applications," Proceedings of the TMS Annual Meeting 2001, 3–15 (2001).*
5. *Bruck, H.A., McNeill, S.R., Sutton, M.A., and Peters, W.H., "Digital Image Correlation Using Newton–Raphson Method of Partial Differential Corrections," EXPERIMENTAL MECHANICS,* **29***, 261–267 (1989).*
6. *James, M.R., Morris, W.L., and Cox, B.N., "A High Accuracy Automated Strain-Field Mapper," EXPERIMENTAL MECHANICS,* **30***, 60–67 (1990).*

7. Franke, E.A., Wenzel, D.J., and Davison, D.L., "Measurement of Microdisplacements by Machine Vision Photogrammetry," Review of Scientific Instruments, **62** (5), 1270–1279 (1991).

8. Noh, S. and Yamaguchi, I., "Two-dimensional Measurement of Strain Distribution by Speckle Correlation," Japanese Journal of Applied Physics, **31**, L1299–L1301 (1992).

9. Chen, D.J., Chiang, F.P., Tan, Y.S., and Don, H.S, "Digital Speckle-displacement Measurement Using a Complex Spectrum Method," Applied Optics, **32**, 1839–1849 (1993).

10. Vendroux, G. and Knauss, W.G., "Submicron Deformation Field Measurements, Part 2. Improved Digital Image Correlation," EXPERIMENTAL MECHANICS, **38** (2), 86–91 (1998).

11. Tong, W., "Detection of Plastic Deformation Patterns in a Binary Aluminum Alloy," EXPERIMENTAL MECHANICS, **37** (4), 452–459 (1997).

12. Tong, W., "Strain Characterization of Propagative Deformation Bands," Journal of Mechanics and Physics of Solids, **46** (10), 2087–2102 (1998).

13. Smith, B.W., Li, X., and Tong, W., "Error Assessment for Strain Mapping by Digital Image Correlation," Experimental Techniques, **22** (4), 19–21 (1998).

14. Tong, W. and Li, X., "Evaluation of Two Plastic Strain Mapping Methods," Proceedings of SEM Annual Conference on Theoretical, Experimental and Computational Mechanics, Cincinnati, OH, June 7–9, 23–26 (1999).

15. Li, X., Spatial Characterization of Unstable Plastic Flows in Two Aluminum Alloys, PhD Thesis, Department of Mechanical Engineering, Yale University, New Haven, CT (2001).

16. Read, D.T., Cheng, Y.-W., Zhang, D., Tong, W., Broggiato, G.B., and Schreier, H., "Results of a Mini Round Robin on Digital Image Correlation," Proceedings of SEM Annual Conference on Theoretical, Experimental and Computational Mechanics (2002).

17. Tong, W. and Zhang, N., "An Experimental Study of Necking in Thin Sheets," Proceedings of the Symposium on Manufacturing Technologies, MED Vol. 12, 2001 ASME Annual Meeting, New York, November (2001).

18. McNeill, S.R., Sutton, M.A., Miao, Z., and Ma, J., "Measurement of Surface Profile Using Digital Image Correlation," EXPERIMENTAL MECHANICS, **37** (1), 13–20 (1997).

19. Helm, J.D., McNeill, S.R., and Sutton, M.A., "Improved Three-dimensional Image Correlation for Surface Displacement Measurement," Optical Engineering, **35** (7), 1991–1920 (1998).

20. Andresen, K., "Strain Tensor for Large Three-dimensional Surface Deformation of Sheet Metal From an Object Grating," EXPERIMENTAL MECHANICS, **39**(1), 30–35 (1999).

21. Li, X. and Tong, W., "Calibration of Digital Imaging Systems for 2D and 3D Applications," Proceedings of 2000 SEM IX International Congress on Experimental Mechanics, Orlando, FL, June 5–8, 598–601 (2000).

22. Lu, H., Vendroux, G., and Knauss, W.G., "Surface Deformation Measurements of a Cylindrical Specimen by Digital Image Correlation," EXPERIMENTAL MECHANICS, **37**(4), 433–439 (1997).

23. Brandon, D. and Kaplan, W.D., Microstructural Characterization of Materials, Wiley, New York, 243–249 (1999).

24. Zhang, N. and Tong, W., "Quantitative Fracture Surface Topography Measurements of an Aluminum Alloy Part," Technical Report, Department of Mechanical Engineering, Yale University, New Haven, CT (2002).